# A battle of designs: triangular vs. L-shaped detectors and parity violation in the gravitational-wave background

Hannah Duval, 1, \* Charles Badger, 2, † and Mairi Sakellariadou<sup>2, ‡</sup>

<sup>1</sup>Theoretische Natuurkunde, Vrije Universiteit Brussel, Pleinlaan 2, B-1050 Brussels, Belgium 
<sup>2</sup>Theoretical Particle Physics and Cosmology Group, Physics Department, 
King's College London, University of London, Strand, London WC2R 2LS, United Kingdom 
(Dated: November 24, 2025)

We investigate the prospects for detecting a parity-violating gravitational-wave background (GWB) with third-generation ground-based detector networks. We focus on a network consisting of one Einstein Telescope (ET) and two Cosmic Explorer (CE) detectors. In our analysis we vary the ET design, detector orientations, and arm lengths, in order to assess the impact of geometry and scale on detection capabilities. We demonstrate that networks with an L-shaped ET design have stronger parity violation constraining power than networks with a triangular ET design, particularly seen when studying ET designs on their own.

# I. INTRODUCTION

The superposition of independent gravitational waves (GW) of cosmological and astrophysical origin forms a gravitational-wave background (GWB). The detection of such a background can shed light on early-universe mechanisms, such as inflation [1–3], first-order phase transitions [4–8], and cosmic strings [9–11], and aid in characterizing astrophysical compact binary coalescences (CBCs) sources and populations [12]. Searches for an unpolarized GWB using data from the ground-based interferometers LIGO [13] and Virgo [14] have placed upper limits on its energy density [15].

A multitude of mechanisms in the early universe can generate parity violation (PV) [16] that results in the production of asymmetric amounts of right- and left-handed circularly polarized GWs. Parity-violating sources and their effects on the GWB have been studied in the literature, including those arising from the Chern-Simons modification to gravity [17–19] and from axion inflation [20, 21], turbulence in the primordial plasma [22–24], or by primordial magnetic fields coupled to the cosmological plasma [25–29].

Probing for polarization in the GWB can place constraints on parity-violating theories [30]. Parity-violating effects in the GWB have been studied in the context of current and future detector sensitivities [31–39], and have been constrained through analyses of LIGO–Virgo data [30, 37, 40].

While PV detection appears unlikely in presently existing ground detectors, third-generation detectors show promise in detecting, or at least imposing tighter constraints in circular polarization. The choice of the detector network configuration will play a crucial role in the circular polarization detection prospects. In this study, we present a dual *theoretical* (based on signal-to-noise ratio) and *data-driven* (Bayesian) analysis for assessing the sensitivity of third-generation ground-based detector networks to parity-violating signatures in a general power-law GWB model.

# II. FORMALISM

The right- and left-handed modes, defined through the circularly polarized bases  $e^{\rm R}=(e^++ie^\times)/\sqrt{2}$  and  $e^{\rm L}=(e^+-ie^\times)/\sqrt{2}$  (with + and × the plus and cross polarizations, respectively) read  $h_{\rm R}=(h_+-ih_\times)/\sqrt{2}$  and  $h_{\rm L}=(h_++ih_\times)/\sqrt{2}$ .

Right- and left-handed correlators are

$$\begin{pmatrix} \langle h_{R}(f,\hat{\Omega})h_{R}^{*}(f',\hat{\Omega}')\rangle \\ \langle h_{L}(f,\hat{\Omega})h_{L}^{*}(f',\hat{\Omega}')\rangle \end{pmatrix} = \frac{\delta(f-f')\delta^{2}(\hat{\Omega}-\hat{\Omega}')}{4\pi} \begin{pmatrix} I(f,\hat{\Omega})+V(f,\hat{\Omega}) \\ I(f,\hat{\Omega})-V(f,\hat{\Omega}) \end{pmatrix},$$
(1)

where  $\langle \cdot \rangle$  is the ensemble average and I,V are the Stokes parameters; V characterizes the asymmetry between right-and left-handed polarized waves, and  $I(\geq |V|)$  is the gravitational wave's total amplitude. The polarization degree  $\Pi(f) = V(f)/I(f) \in [-1,1]$ , with  $\Pi = -1$  and  $\Pi = +1$  defining fully left- and right-handed polarization, respectively, while  $\Pi = 0$  stands for an unpolarized isotropic GWB. For the latter (V=0), Eq. (1) reduces to the standard correlator for an unpolarized isotropic background. The signal-to-noise ratios (SNRs)  $\rho_I$  and  $\rho_V$  for the I- and V-modes, respectively, of a circularly polarized GWB, are calculated for a detector network over an observing time T [41]. The power-law integrated (PI) curve,  $\Omega_{\mathrm{PI},I}$ , characterizes a detector network's I-mode sensitivity [42]. We extend the procedure to the V-mode to obtain the PI sensitivity curve,  $\Omega_{\mathrm{PI},V}$ , for the V-mode.

To search for parity-violating GWBs, we adapt the formalism described in [41, 43] to third-generation ground-based detector networks.

# III. PARITY VIOLATING MODELS

We explore the parity-violation detection prospects of the modified GWB spectrum from formalism [30, 43]

$$\Omega'_{\rm GW}(f) = \Omega_{\rm GW}(f) \left[ 1 + \Pi(f) \frac{\gamma_V^{d_1 d_2}(f)}{\gamma_I^{d_1 d_2}(f)} \right],$$
(2)

<sup>\*</sup> Hannah.Marie.D.Duval@vub.be

<sup>†</sup> charles.badger@kcl.ac.uk

<sup>&</sup>lt;sup>‡</sup> mairi.sakellariadou@kcl.ac.uk

as it would appear in the detector pairs  $d_1$ ,  $d_2$  where  $\gamma_{I/V}^{d_1d_2}$  are the normalized overlap reduction functions for the I- and V-modes calculated via analytical and numerical methods [44, 45] defined as the usual

$$\gamma_I^{d_1 d_2}(f) = \frac{5}{8\pi} \int d\hat{\Omega} (F_{d_1}^+ F_{d_2}^{+*} + F_{d_1}^{\times} F_{d_2}^{\times *}) e^{2\pi i f \hat{\Omega} \Delta \overrightarrow{x}} , \quad (3)$$

$$\gamma_V^{d_1 d_2}(f) = -\frac{5i}{8\pi} \int d\hat{\Omega} (F_{d_1}^+ F_{d_2}^{\times *} - F_{d_1}^{\times} F_{d_2}^{+*}) e^{2\pi i f \hat{\Omega} \Delta \overrightarrow{x}} ,$$
(4)

for beam pattern function  $F_d^A$  for the usual  $A=+,\times$  polarizations.

We assume a general power-law GWB spectrum  $\Omega_{\rm GW}=\Omega_{\alpha}(f/f_{\rm ref})^{\alpha}$  parametrized by amplitude  $\Omega_{\alpha}$  and spectral index  $\alpha$  [37]; we set the reference frequency  $f_{\rm ref}=25$  Hz. Theoretically motivated polarized GWBs can be modeled by specific choices of  $\alpha$ , with the polarization typically assumed constant for simplicity. For instance, GWBs sourced by non-Abelian axion inflation [3, 46], string-inspired cosmology models [17], and some turbulence models [47] can be well-modeled by a power-law GWB with constant polarization. In what follows, we adopt this assumption,  $\Pi(f)={\rm const.}$ , noting that the framework can be generalized to arbitrary polarized GWBs, for example, a frequency-dependent power-law  $\Pi(f)$  model [37].

# IV. FUTURE GROUND-BASED DETECTOR CONFIGURATIONS

We consider seven representative networks, each combining one Einstein Telescope (ET) with two Cosmic Explorer (CE) detectors, using the geometric information from [48]. We include triangular ET designs with 10 and 15 km arms  $(\Delta_{10}, \Delta_{15})$ , as well as ET designs consisting of two L-shaped interferometers with 15 km arms (S, R). For CE, we consider L-shaped detectors with 20 km (P) and 40 km (Y) arms. The triangular configurations consist of three interferometers, while an L-shaped detector consists of one interferometer. Thus a  $\Delta$  + (PY) network contains five detectors (10 baselines), while an (SR) + (PY) network contains four (6 baselines). These configurations explore how detector orientations and arm length influence network performance, with some optimized for GWB sensitivity and others for CBC source localization, clarifying whether differences between triangular and L-shaped designs arise from geometry or arm length. Further technical details are in [48], for which we use the amplitude spectral density curves found in [49] and [50], and the full set of configuration names and descriptions is in Table I.

In Fig. 1, we present the I- and V-mode PI curves for the various network configurations. The  $\Omega_{\text{PI},I}$  curves show that GWB-optimized networks yield the highest I-mode sensitivity, which is expected by construction. In particular,  $(\text{SR})_1(\text{PY})_1$  dominates below  $\sim 40$  Hz, while at higher frequencies the 15 km triangular configurations,  $\Delta_{15}(\text{PY})_4$  and  $\Delta_{15}(\text{PY})_5$ , outperform the 2L designs.

Network name	Description	
$\Delta_{10}(PY)_4$	10 km $\Delta$ + 2CE, GWB-optimized	
$\Delta_{10}(PY)_5$	$10 \text{ km } \Delta + 2 \text{CE}$ , Localization-optimized	
$\Delta_{15}(PY)_4$	15 km $\Delta$ + 2CE, GWB-optimized	
$\Delta_{15}(PY)_5$	15 km $\Delta$ + 2CE, Localization-optimized	
$(SR)_1(PY)_1$	15 km 2L + 2CE, GWB-optimized	
$(SR)_2(PY)_2$	15 km 2L + 2CE, Localization-optimized	
$(SR)_3(PY)_3$	15 km 2L + 2CE, Hybrid	

TABLE I: The different third-generation detector network configurations that are considered in this study, which follow the definitions and optimization procedures of [48]. "GWB-optimized" denotes configurations favoring GWB sensitivity and are determined using a PI-curve method, while "Localization-optimized" configurations favor source localization and are computed using the network-alignment factor. "Hybrid" configurations provide a balanced design providing a trade-off between the two.

The  $\Omega_{{\rm PI},V}$  curves exhibit reduced sensitivity compared to their I-mode counterparts, with sensitivity decreasing as  $|\Pi|$  approaches 0. Their ranking is relatively stable across frequencies: below 20 Hz,  $({\rm SR})_3({\rm PY})_3$  is most sensitive and  $\Delta_{10}({\rm PY})_5$  least, while above 25 Hz the best sensitivity shifts to  $({\rm SR})_1({\rm PY})_1$ , with  $\Delta_{10}({\rm PY})_5$  remaining the weakest.

This result is expected since the co-planar triangular ET detectors are weak to V-modes [35, 38, 41] and weaken a network's overall sensitivity to PV detection in comparison to networks with 2L ET designs that are spatially separated. This was verified with a separate study in which the PV detection prospects of ET alone were examined, and find that present constraints [40] have ruled out the parameter space for which ET detector can detect circular polarization, thus the inclusion of CE detectors is a necessity to make proper parity-violation inferences. See Appendix A for further details.

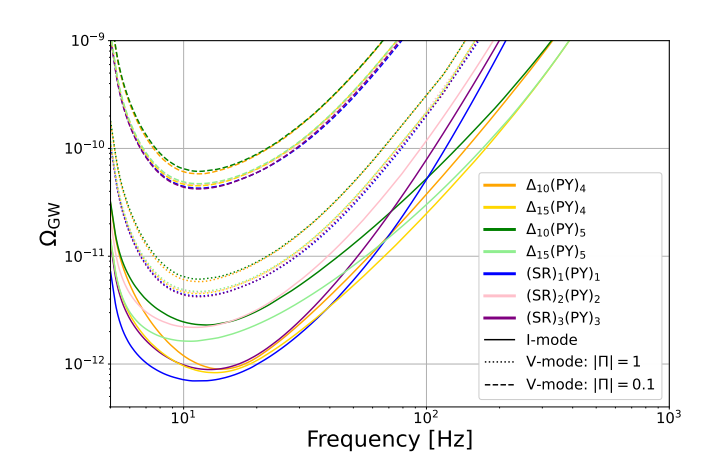


FIG. 1: PI sensitivity curves for I-mode (solid lines) and V-mode (dotted and dashed lines), shown for the seven different detector third-generation network configurations for an observing time of one year and  $\rho=4$ . The V-mode curves correspond to  $|\Pi|=1$  (dotted) and  $|\Pi|=0.1$  (dashed).

#### V. FUTURE DETECTION PROSPECTS

We present theoretical (based on signal-to-noise ratio) and data-driven (obtained with a Bayesian analysis) prospects for detecting PV by applying the previously described formalisms to third-generation detector networks. Our analysis covers general power-law GWBs with  $-12.5 \leq \log_{10} \Omega_{\alpha} \leq -10$ , spectral indices  $\alpha = -3, \ldots, 3$ , and polarization degrees  $-1 \leq \Pi \leq 1$ . We note that the upper bound on the  $\log_{10} \Omega_{\alpha}$  range is determined by current detector constraints [15], while the lower bound is to allow studied GWBs to be potentially detected in the considered networks, as seen in Fig. 1.

# A. Signal-to-noise ratio

The sensitivities of the third-generation detector networks are quantified by the I- and V-mode SNRs. Figure 2 shows the results for a flat PL ( $\alpha=0$ ) spectrum across the seven network configurations. As expected,  $\rho_I$  is independent of  $\Pi$  and scales only with the GWB amplitude, while  $\rho_V$  grows with  $|\Pi|$ , enhancing detectability for more strongly polarized backgrounds. We repeat this study for other power-law indices and rank their detection prospects in Tables II and III.

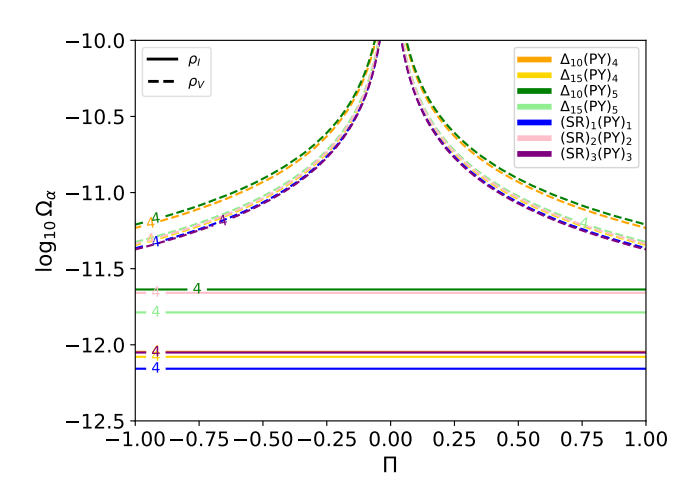


FIG. 2: SNRs for I-mode (solid lines) and V-mode (dashed lines) for the seven third-generation detector network configurations, assuming a flat ( $\alpha = 0$ ) power-law GWB.

We find that the 2L network  $(SR)_1(PY)_1$  provides the largest  $\rho_I$  for  $-3 \le \alpha \le 2$ , while the 15 km triangular network  $\Delta_{15}(PY)_4$  overtakes it at  $\alpha=3$ , highlighting the advantage of a triangular design for GWBs with large positive spectral indices. For the V-mode,  $(SR)_3(PY)_3$  is most sensitive for  $-3 \le \alpha \le 1$ , with  $(SR)_1(PY)_1$  dominating at larger indices. Among triangular ETs, longer arms  $(\Delta_{15}(PY)_{4,5})$  outperform their 10 km counterparts, confirming that arm length impacts sensitivity. Nevertheless, networks incorporating a 2L ET design consistently achieve the highest  $\rho_V$ , as these networks have non-vanishing  $\gamma_V^{d_1d_2}$ , which significantly enhance sensitivity to the V-mode. To verify that this enhancement is intrinsic to the ET geometry rather than the CE ori-

$\alpha$	-3, -2	-1, 0	$\frac{1}{2}, \frac{2}{3}, 1, 2$	3
1st	$(SR)_1(PY)_1$	$(SR)_1(PY)_1$	$(SR)_1(PY)_1$	$\Delta_{15}(PY)_4$
2nd	$(SR)_3(PY)_3$	$\Delta_{15}(PY)_4$	$\Delta_{15}(PY)_4$	$\Delta_{15}(\mathrm{PY})_5$
3rd	$\Delta_{15}(PY)_4$	$(SR)_3(PY)_3$	$\Delta_{10}(PY)_4$	$\Delta_{10}(\mathrm{PY})_4$
4th	$\Delta_{15}(PY)_5$	$\Delta_{10}(PY)_4$	$(SR)_3(PY)_3$	$\Delta_{10}(PY)_5$
5th	$\Delta_{10}(PY)_4$	$\Delta_{15}(PY)_5$	$\Delta_{15}(PY)_5$	$ (SR)_1(PY)_1 $
6th	$(SR)_2(PY)_2$	$(SR)_2(PY)_2$	$\Delta_{10}(PY)_5$	$(SR)_3(PY)_3$
7th	$\Delta_{10}(PY)_5$	$\Delta_{10}(\text{PY})_5$	$(SR)_2(PY)_2$	$(SR)_2(PY)_2$

TABLE II: Ranking from best (1st) to worst (7th) of detector networks by I-mode SNRs for different PL indices  $\alpha$ .

$\alpha$	-3 to $1$	2,3
1st	$(SR)_3(PY)_3$	$(SR)_1(PY)_1$
2nd	$(SR)_1(PY)_1$	$(SR)_3(PY)_3$
3rd	$\Delta_{15}(PY)_4$	$(SR)_2(PY)_2$
4th	$(SR)_2(PY)_2$	$\Delta_{15}(PY)_4$
5th	$\Delta_{15}(PY)_5$	$\Delta_{15}(PY)_5$
6th	$\Delta_{10}(PY)_4$	$\Delta_{10}(PY)_4$
7th	$\Delta_{10}(PY)_5$	$\Delta_{10}(PY)_5$

TABLE III: Ranking from best (1st) to worst (7th) of detector networks by V-mode SNRs for different PL indices  $\alpha$ .

entation, Appendix A presents ET-only configurations. These results confirm that triangular ETs suffer a dramatic loss of PV sensitivity compared to 2L designs. Hence, optimal PV detection requires an ET with a 2L design, highlighting that detector geometry is the dominant factor for detecting parity-violating signals. These results are consistent with the PI curves, whose frequency-dependent shapes qualitatively explain the SNR rankings across different spectral indices. We highlight that fixing different reference frequencies result in the same ordering of SNR prospects, emphasizing the generality of our results.

# B. Bayesian analysis

We now complement the SNR analysis with a data-driven Bayesian analysis on simulated signals, assuming the design sensitivity and noise characteristics of each third-generation network configuration. Parameter estimation is carried out with the pygwb [51] and Bilby [52] packages using the Dynesty sampler. This allows us to assess a network's capability to detect a polarized signal and to distinguish it from an unpolarized one. To this end, we fix a power-law index  $\alpha$  and generate 1600 simulated injections uniformly over the  $\log_{10}\Omega_{\alpha}$  and  $\Pi$  range in each network configuration, then searching over the priors of Table IV based off of theoretical bounds and previously explored search priors [40, 53]. The procedure is then repeated with  $\Pi = 0$  to model unpolarized backgrounds, using the same amplitude and spectral index priors. To reduce statistical noise, we generate 15 independent injection sets with random detector noise and combine results with an optimized weighted average [44]. This enables a direct comparison between polarized and unpolarized searches.

Parameters $\theta$	Priors
$\log_{10} \Omega_{\alpha}$	Uniform(-18, -7)
$\alpha$	Gaussian(0, 3.5)
П	Uniform(-1,1)

TABLE IV: Priors used in the Bayesian analysis. The  $\log_{10}\Omega_{\alpha}$  and  $\alpha$  priors follow previous searches, while taking into account the sensitivity of third-generation detectors [53, 54]. The prior on  $\Pi$  is the full, physically allowed range of values [37].

# 1. Comparison to signal-to-noise

We compare the recovered data-analysis Bayes factors to the I- and V-mode SNRs for all injections. Figure 3 shows this comparison for the most optimistic  $((SR)_3(PY)_3)$  and most pessimistic  $(\Delta_{10}(PY)_5)$  network configurations for a flat GWB spectrum. More concretely, it shows the SNRs alongside the log Bayes factors for a polarized model compared to detector noise,  $\ln \mathcal{B}_{\text{Noise}}^{\Pi\neq 0}$ , and to an unpolarized model,  $\ln \mathcal{B}_{\Pi=0}^{\Pi\neq 0}$ . We adopt strong detection thresholds of  $\ln \mathcal{B}_{\text{Noise}}^{\Pi\neq 0}$  and  $\ln \mathcal{B}_{\Pi=0}^{\Pi\neq 0}$  equal to 8. These correspond to  $\rho_I$  and  $\rho_V$  equal to 4, since  $\rho^2 \simeq 2 \ln \mathcal{B}$  in the strong signal regime [44]. Our findings confirm this relation. In conclusion, the SNR pre-

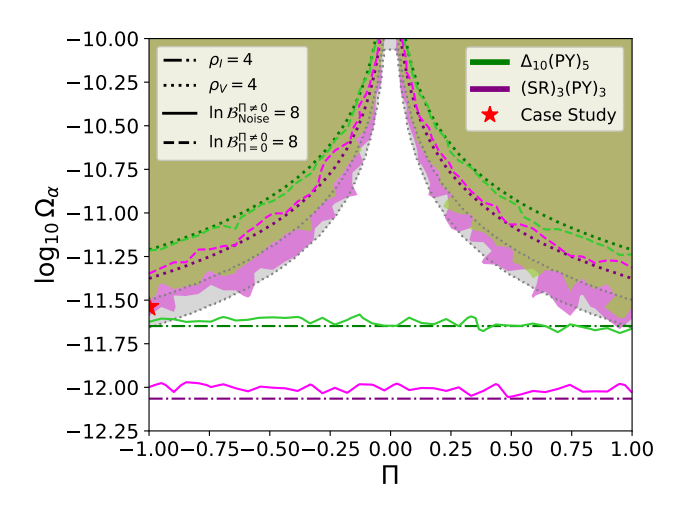


FIG. 3: SNR and log Bayes detection prospects for I- and V-modes in a flat GWB in the  $\Delta_{10}(\text{PY})_5$  and  $(\text{SR})_3(\text{PY})_3$  configurations. The green and purple filled regions correspond to 95% exclusion regions of  $\Pi=0$ . The gray-shaded region indicates where  $\rho_V^{\Delta_{10}(\text{PY})_5} \leq \rho_V^{95\%, \text{ crit}} \leq \rho_V^{(\text{SR})_3(\text{PY})_3}$ , where  $\rho_V^{95\%, \text{ crit}} = 2.16$  is the approximate V-mode SNR where  $\Pi=0$  is excluded at 95%. The red star marks the case study discussed in Sec. VB 2.

dictions reproduce the trends seen in the data-driven analysis across both network extremes, demonstrating that simple theoretical estimates based on SNRs provide an excellent guide to the detectability of polarized GWBs.

#### 2. Parameter estimation

We perform a Bayesian analysis to assess parameter recovery of simulated parity-violating GWBs for the most optimistic,  $(\text{SR})_3(\text{PY})_3$  and most pessimistic,  $\Delta_{10}(\text{PY})_5$ , network configurations. From the marginalized posteriors, we compute the 95% Upper Limits (UL) and Lower Limits (LL) on  $\Pi$ , allowing us to make  $\Pi=0$  exclusion analyses. This is shown in Fig. 3: purple and green regions denote where  $\Pi=0$  is ruled out with at least 95% confidence by the 2L and triangular networks, respectively. We define a threshold region as the parameter space where the 2L network excludes  $\Pi=0$  at 95% confidence, but the triangle network does not. An average V-mode SNR corresponding to the borders of this threshold region is  $\rho_V^{\Delta_{10}(\text{PY})_5} \leq 2.16 \leq \rho_V^{(\text{SR})_3(\text{PY})_3}$ , which is indicated by the gray-shaded region in Fig. 3.

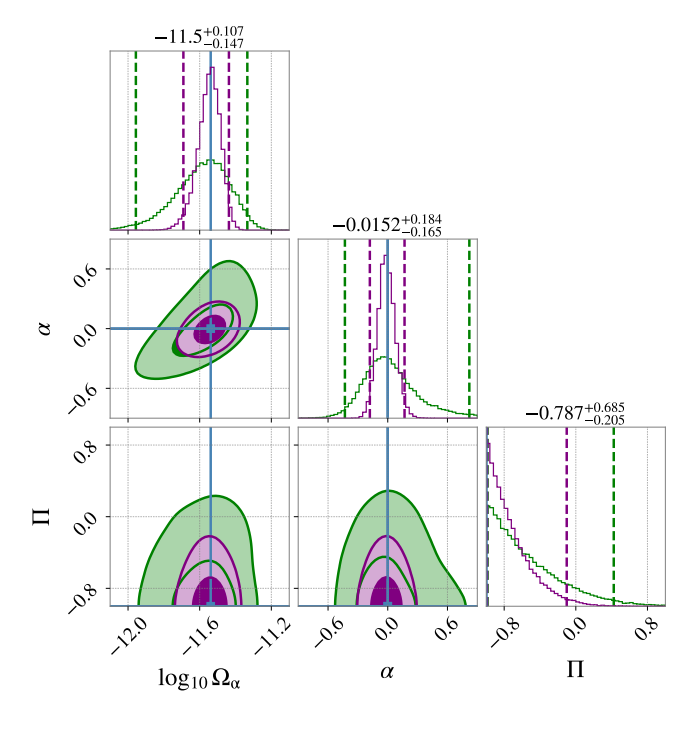


FIG. 4: Posterior distributions from Bayesian inference for parity-violating power-law GWBs, combined over 15 simulated runs for  $f_{\rm ref}=25$  Hz. Shown are the (SR)<sub>3</sub>(PY)<sub>3</sub> (purple) and  $\Delta_{10}$ (PY)<sub>5</sub> (green) networks, with dark and light shading indicating  $1\sigma$  and  $2\sigma$  credible regions. Here:  $\Pi=-1$  and  $\log_{10}\Omega_{\alpha}=-11.54$  shown in blue.

Next, we focus on a flat parity-violating GWB case study with  $\log_{10}\Omega_{\alpha}=-11.54,\,\Pi=-1,$  indicated by the red star in Fig. 3. These parameters were chosen so that the signal lies in the threshold regime. The combined posteriors results are shown in Fig. 4, where model parameters are recovered

within  $1\sigma$  for both networks. We derive the 95% UL on  $\Pi$  equal to -0.238 and 0.233 for the 2L and triangular network, respectively. We also compute log Bayes factors for the parity-violating and the unpolarized GWB searches. For the  $(SR)_3(PY)_3$  network, we obtain  $\ln \mathcal{B}_{\Pi=0}^{\Pi\neq 0}=2.914\pm0.043,$  while for  $\Delta_{10}(PY)_5$  we find  $\ln \mathcal{B}_{\Pi=0}^{\Pi\neq 0}=0.946\pm0.037,$  highlighting the greater capability of  $(SR)_3(PY)_3$  to distinguish a polarized from unpolarized GWBs than  $\Delta_{10}(PY)_5.$  Although these log Bayes factors do not indicate a strong preference for a PV model, this injection demonstrates that  $(SR)_3(PY)_3$  can rule out  $\Pi=0$  at the 95% confidence level, while  $\Delta_{10}(PY)_5$  cannot.

In conclusion, these findings highlight that network design strongly impacts parameter constraints, particularly for circular polarization  $\Pi$ , with the 2L network providing tighter constraints on parity-violating GWBs.

#### VI. CONCLUSIONS

In this study, the detection prospects of a general parity-violating GWB with third-generation detector networks were investigated using a signal-to-noise ratio and a Bayesian analysis approach. By extending the standard GWB formalism to include the *V*-mode, we introduced PI curves and SNR prospects that accurately reproduce data-based results, providing an efficient proxy for assessing circular polarization detection prospects.

We considered an ET detector, in both triangular and 2L designs, paired with two CE detectors across a range of orientations, and ET arm lengths. A broad set of power-law GWB spectra, motivated by cosmological parity-violating mechanisms, was analyzed.

Across all scenarios, ET in 2L configurations are consistently more sensitive to parity violation than triangular ET configurations, with the gap most pronounced for standalone ET. Parameter estimation studies further demonstrate that network design strongly affects the ability to constrain the GWB parameters. We find that an optimal network design choice can tighten a searched parameter space and can place polarization bounds that exclude  $\Pi=0$  at 95% compared to alternative detector designs. In Appendix A, we show that parity violation detection in ET alone has been ruled out; circular polarization in a third-generation network requires CE detectors.

These findings underscore the importance of a global network design choices in order to optimize the discovery potential for fundamental physics in the GWB. These results highlight how next-generation detectors could open a direct observational window onto fundamental parity-violating physics in the early Universe.

# ACKNOWLEDGMENTS

We thank Michael Ebersold for valuable discussions on third-generation network configurations, Alberto Mariotti and Miguel Vanvlasselaer for helpful discussions. We are also thankful to Gianmassimo Tasinato and Angelo Ricciardone for useful comments. This document has an ET document number ET-0483A-25. The work of MS is partially supported by the Science and Technology Facilities Council (STFC grant ST/X000753/1). HD is supported by the Strategic Research Program High-Energy Physics of the Research Council of the Vrije Universiteit Brussel, the iBOF "Unlocking the Dark Universe with Gravitational Wave Observations: from Quantum Optics to Quantum Gravity" of the Vlaamse Interuniversitaire Raad.

- [1] L. P. Grishchuk, Zh. Eksp. Teor. Fiz. 67, 825 (1974).
- [2] A. A. Starobinsky, JETP Lett. **30**, 682 (1979).
- [3] C. Badger, H. Duval, T. Fujita, S. Kuroyanagi, A. Romero-Rodríguez, and M. Sakellariadou, Phys. Rev. D 110, 084063 (2024), arXiv:2406.11742 [astro-ph.CO].
- [4] M. Kamionkowski, A. Kosowsky, and M. S. Turner, Phys. Rev. D 49, 2837 (1994), arXiv:astro-ph/9310044.
- [5] R. Apreda, M. Maggiore, A. Nicolis, and A. Riotto, Nucl. Phys. B 631, 342 (2002), arXiv:gr-qc/0107033.
- [6] C. Grojean and G. Servant, Phys. Rev. D 75, 043507 (2007), arXiv:hep-ph/0607107.
- [7] A. Romero, K. Martinovic, T. A. Callister, H.-K. Guo, M. Martínez, M. Sakellariadou, F.-W. Yang, and Y. Zhao, Phys. Rev. Lett. 126, 151301 (2021), arXiv:2102.01714 [hep-ph].
- [8] C. Badger et al., Phys. Rev. D 107, 023511 (2023), arXiv:2209.14707 [hep-ph].
- [9] P. Auclair et al., JCAP 04, 034 (2020), arXiv:1909.00819 [astro-ph.CO].
- [10] T. Damour and A. Vilenkin, Phys. Rev. D 64, 064008 (2001), arXiv:gr-qc/0104026.
- [11] R. Abbott et al. (LIGO Scientific, Virgo, KAGRA), Phys. Rev. Lett. 126, 241102 (2021), arXiv:2101.12248 [gr-qc].
- [12] R. Abbott <u>et al.</u> (KAGRA, VIRGO, LIGO Scientific), Phys. Rev. X **13**, 011048 (2023), arXiv:2111.03634 [astro-ph.HE].
- [13] J. Aasi et al. (LIGO Scientific), Class. Quant. Grav. 32, 074001 (2015), arXiv:1411.4547 [gr-qc].
- [14] F. Acernese et al. (VIRGO), Class. Quant. Grav. 32, 024001 (2015), arXiv:1408.3978 [gr-qc].
- [15] A. G. Abac et al. (LIGO Scientific, VIRGO, KAGRA), (2025), arXiv:2508.20721 [gr-qc].
- [16] S. H. S. Alexander, M. E. Peskin, and M. M. Sheikh-Jabbari, Physical Review Letters 96 (2006), 10.1103/physrevlett.96.081301.
- [17] M. Satoh, S. Kanno, and J. Soda, Physical Review D 77 (2008), 10.1103/physrevd.77.023526.
- [18] N. Bartolo, L. Caloni, G. Orlando, and A. Ricciardone, Journal of Cosmology and Astroparticle Physics 2021, 073 (2021).
- [19] T. Takahashi and J. Soda, Phys. Rev. Lett. 102, 231301 (2009).
- [20] N. Barnaby and M. Peloso, Physical Review Letters 106 (2011), 10.1103/physrevlett.106.181301.
- [21] E. Dimastrogiovanni and M. Peloso, Physical Review D 87 (2013), 10.1103/physrevd.87.103501.
- [22] M. Kamionkowski, A. Kosowsky, and M. S. Turner, Physical Review D 49, 2837–2851 (1994).
- [23] E. Witten, Phys. Rev. D 30, 272 (1984).
- [24] C. J. Hogan, MNRAS 218, 629 (1986).
- [25] A. Brandenburg, K. Enqvist, and P. Olesen, Physical Review D 54, 1291–1300 (1996).
- [26] M. Christensson, M. Hindmarsh, and A. Brandenburg, Physical Review E 64 (2001), 10.1103/physreve.64.056405.
- [27] T. Kahniashvili, A. Brandenburg, A. G. Tevzadze, and B. Ratra, Physical Review D 81 (2010), 10.1103/physrevd.81.123002.
- [28] A. Brandenburg, T. Kahniashvili, S. Mandal, A. R. Pol, A. G. Tevzadze, and T. Vachaspati, Physical Review Fluids 4 (2019), 10.1103/physrevfluids.4.024608.
- [29] A. Brandenburg, Y. He, T. Kahniashvili, M. Rheinhardt, and J. Schober, (2021), arXiv:2101.08178 [astro-ph.CO].
- [30] S. Crowder, R. Namba, V. Mandic, S. Mukohyama, and M. Peloso, Physics Letters B 726, 66–71 (2013).
- [31] N. Seto, Phys. Rev. D 75, 061302 (2007).
- [32] A. Ricciardone, Journal of Physics: Conference Series 840,

- 012030 (2017).
- [33] G. Orlando, M. Pieroni, and A. Ricciardone, Journal of Cosmology and Astroparticle Physics 2021, 069 (2021).
- [34] N. Bartolo, V. Domcke, D. G. Figueroa, J. García-Bellido, M. Peloso, M. Pieroni, A. Ricciardone, M. Sakellariadou, L. Sorbo, and G. Tasinato, JCAP 11, 034 (2018), arXiv:1806.02819 [astro-ph.CO].
- [35] V. Domcke, J. García-Bellido, M. Peloso, M. Pieroni, A. Ricciardone, L. Sorbo, and G. Tasinato, Journal of Cosmology and Astroparticle Physics 2020, 028–028 (2020).
- [36] P. Xu, Z. Wang, and L.-E. Qiang, Physics Letters B 789, 378 (2019).
- [37] K. Martinovic, C. Badger, M. Sakellariadou, and V. Mandic, Phys. Rev. D 104, L081101 (2021), arXiv:2103.06718 [gr-qc].
- [38] C. Badger and M. Sakellariadou, (2021), arXiv:2112.04650 [gr-qc].
- [39] N. M. J. Cruz, A. Malhotra, G. Tasinato, and I. Zavala, Phys. Rev. D 110, 103505 (2024), arXiv:2406.04957 [astro-ph.CO].
- [40] A. G. Abac et al. (LIGO Scientific, VIRGO, KAGRA), (2025), arXiv:2510.26848 [gr-qc].
- [41] N. Seto and A. Taruya, Phys. Rev. D 77, 103001 (2008), arXiv:0801.4185 [astro-ph].
- [42] E. Thrane and J. D. Romano, Phys. Rev. D 88, 124032 (2013), arXiv:1310.5300 [astro-ph.IM].
- [43] N. Seto and A. Taruya, Phys. Rev. Lett. 99, 121101 (2007).
- [44] J. D. Romano and N. J. Cornish, Living Reviews in Relativity 20 (2017), 10.1007/s41114-017-0004-1.
- [45] I. Caporali and A. Ricciardone, (2025), arXiv:2507.15791 [astro-ph.IM].
- [46] A. Maleknejad, JHEP 07, 104 (2016), arXiv:1604.03327 [hep-ph].
- [47] T. Kahniashvili, G. Gogoberidze, and B. Ratra, Physical Review Letters 95 (2005), 10.1103/physrevlett.95.151301.
- [48] M. Ebersold, T. Regimbau, and N. Christensen, Phys. Rev. D 110, 122006 (2024), arXiv:2408.06032 [gr-qc].
- [49] S. Danilishin and T. Zhang, "ET sensitivity curves used for CoBA science study," (2023).
- [50] P. Fulda, L. Barsotti, M. Evans, and K. Kuns, CE Document T2000017-v8 (2023).
- [51] A. I. Renzini et al., J. Open Source Softw. 9, 5454 (2024).
- [52] G. Ashton <u>et al.</u>, Astrophys. J. Suppl. **241**, 27 (2019), arXiv:1811.02042 [astro-ph.IM].
- [53] K. Martinovic, P. M. Meyers, M. Sakellariadou, and N. Christensen, Phys. Rev. D 103, 043023 (2021), arXiv:2011.05697 [gr-qc].
- [54] R. Abbott, T. D. Abbott, S. Abraham, F. Acernese, K. Ackley, A. Adams, C. Adams, R. X. Adhikari, V. B. Adya, C. Affeldt, D. Agarwal, and et. al. (LIGO Scientific Collaboration, Virgo Collaboration, and KAGRA Collaboration), Phys. Rev. D 104, 022004 (2021).

# Appendix A: Discussion on Einstein Telescope alone

We briefly assess the detection prospects of a parity violating GWB using ET alone. For this purpose, we consider baselines that differ from those adopted in the main analysis. Specifically, we introduce the notation  $\Delta'_{10}$  and  $\Delta'_{15}$  to denote closed, fully symmetric triangular ET configurations with 10 km and 15 km arms, respectively. These correspond to the idealized case of a perfectly equilateral triangle formed by three co-located interferometers, with each vertex separated by  $60^{\circ}$ . For comparison, we also include the configurations  $\Delta_{10}$  and  $\Delta_{15}$  already used in the main text and defined in [48]. These differ in that the three interferometers do not form an exactly closed triangle. As a result, the  $\Delta_{10}$  and  $\Delta_{15}$  configurations are slightly asymmetric. This asymmetry yields enhanced sensitivity to V-modes, since the chiral ORF is slightly larger than that of a perfectly closed triangle.

In addition to triangular configurations, we also examine two 2L configurations, denoted by  $(SR)_0$  and  $(SR)_{45}$ . The  $(SR)_0$  setup corresponds to the optimal 2L configuration for GWB detection where the two detectors are aligned (relative orientation of  $0^\circ$ ). By contrast, the  $(SR)_{45}$  represents the most pessimistic case for GWB detection, where the detectors are rotated by  $45^\circ$  with respect to one another. It is important to emphasize that  $(SR)_0$  and  $(SR)_{45}$  differ from  $(SR)_1$  and  $(SR)_2$  considered in the main analysis, since the latter were defined relative to the optimal configuration of a global network including two CEs, whereas here the reference is ET alone. In Table V, the latitude and longitude of each network center, the X- and Y-arm endpoints and azimuths are given.

Figure 5 shows the PI curves for both the I- and V-modes across the different ET-only configurations. For comparison, we also include a parity-violating PL GWB with spectral index  $\alpha=0$ , to facilitate direct comparison with the corresponding SNR prospects shown in Fig. 6. The perfectly closed and symmetric triangular configurations  $\Delta'$  exhibit noticeably lower V-mode sensitivity than the slightly asymmetric  $\Delta$  setups used in the main text, illustrating that even small asymmetries in ET's geometry can enhance parity-violation detection. Nevertheless, all triangular configurations, whether symmetric or slightly asymmetric, remain significantly less sensitive to the V-modes than the 2L designs.

We have again performed SNR studies for multiple spectral indices  $\alpha$ . For the I-mode SNRs, the ranking from most to least sensitive is:  $(SR)_0$ ,  $(SR)_{45}$ ,  $\Delta_{15} = \Delta'_{15}$  and  $\Delta_{10} = \Delta'_{10}$ . For the V-mode SNRs, the resulting network rankings are summarized in Tables VI, confirming that 2L configurations consistently outperform triangular ET for V-mode detection. Moreover, current bounds on the parity-violated GWB [40]

have ruled out the parity-violating parameter space that is detectable by both 2L and the  $\Delta$  configurations, as seen in Fig.6. Consequently, if ET were constructed without CE, none of the configurations would be able to detect circularly polarized GWBs at a confident SNR level.

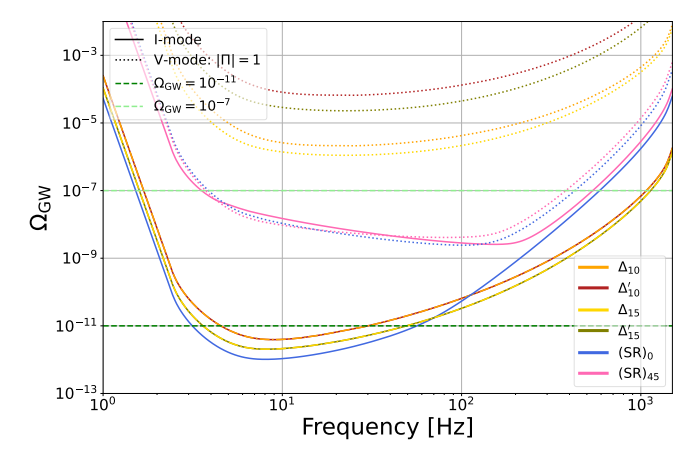


FIG. 5: PI curves sensitivity curves for I-mode (solid lines) and V-mode (dotted and dashed lines), shown for the 6 different ET configurations, for an observing time of one year and  $\rho=4$ . The V-mode curves correspond to  $|\Pi|=1$  (dotted) and  $|\Pi|=0.1$  (dashed). We also show PL GWBs with spectral index of  $\alpha=0$ .

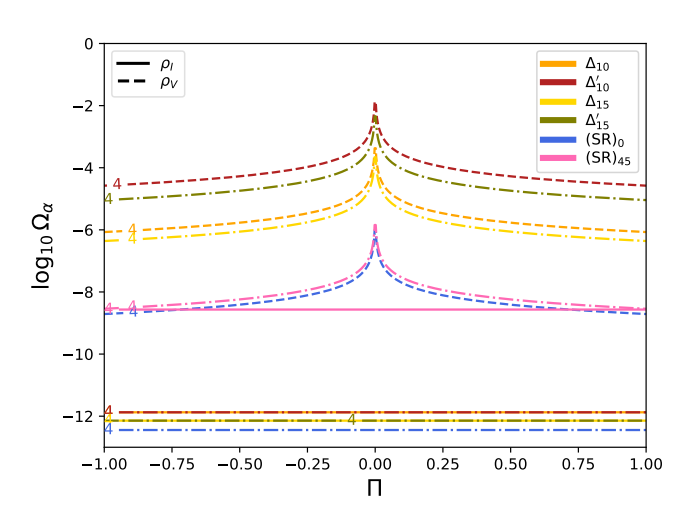


FIG. 6: SNRs for I-mode (solid lines) and V-mode (dashed lines), shown for the five different ET configurations for a PL GWB with  $\alpha=0$ .

Name	Origin (lat, lon)	X-arm end (lat, lon)	Y-arm end (lat, lon)	Azimuth [°] X-/Y-arm
E1'10	43.6300, 10.5000	43.7149, 10.5413	43.6983, 10.4193	19.43 /319.43
E2'10	43.7149, 10.5413	43.6983, 10.4193	43.6300, 10.5000	259.46 /199.46
E3'10	43.6983, 10.4193	43.6300, 10.5000	43.7149, 10.5413	139.37 /79.37
E1'15	43.6300, 10.5000	43.7573, 10.5620	43.7325, 10.3789	19.43 /319.43
E2'15	43.7573, 10.5620	43.7325, 10.3789	43.6300, 10.5000	259.47 /199.47
E3'15	43.7325, 10.3789	43.6300, 10.5000	43.75730, 10.5620	139.35/79.35
$S_0$	40.5200, 9.4170	40.3851, 9.4093	40.5258, 9.2402	182.51/272.51
S <sub>45</sub>	40.5200, 9.4170	40.4203, 9.5364	40.4287, 9.2867	137.51 /227.51
R <sub>0</sub> =R <sub>45</sub>	50.7200, 5.9210	50.8548, 5.9210	50.7198, 6.1334	0.00/90.00

TABLE V: ET coordinates and azimuths (clockwise from North).

$\alpha$	-3, -2, -1	$0, \frac{1}{2}, 1, \frac{2}{3}, 2, 3$
1st	(SR) <sub>45</sub>	$(SR)_0$
2nd	$(SR)_0$	$(SR)_{45}$
3rd	$\Delta_{15}$	$\Delta_{15}$
4th	$\Delta_{10}$	$\Delta_{10}$
5th	$\Delta'_{15}$	$\Delta'_{15}$
6th	$\Delta'_{10}$	$\Delta'_{10}$

TABLE VI: Ranking of ET configurations from most (1st) to least (6th) sensitive for different spectral indices  $\alpha$  for the V-mode SNRs.